Quantum-Dots-Based Phase Separation into a 3D/0D Perovskite Heterojunction for Boosting X-Ray Detector Performance

Han Li,[a,b†] Shanshan Yu,[a,c†] Handong Jin,[a,b†] Zikun Jin,[b] Wei Qian,[b] Wanshun Yang,[b] Shihe Yang[ab]*

Dr. H. Li, S. Yu, H. Jin, Prof. S. Yang

Institute of Biomedical Engineering, Shenzhen Bay Laboratory, Shenzhen, Guangdong 518107, China

chsyang@pku.edu.cn

Dr. H. Li, S. Yu, H. Jin, Z. Jin, Dr. W. Qian, W. Yang, Prof. S. Yang

Guangdong Provincial Key Lab of Nano-Micro Materials Research, School of Advanced Materials, Shenzhen Graduate School, Peking University, Shenzhen, Guangdong 518055, China.

S. Yu,

Department of Chemistry, The University of Hong Kong, Hong Kong S.A.R., China

The current distribution in the dark and light fields of the Pe-FPD was fitted to a normal distribution curve, as reported elsewhere:

$$f(x) = \frac{1}{\sqrt{2\pi}\sigma} exp\left(-\frac{(x-\mu)^2}{2\sigma^2}\right)$$

where μ is the average current value and σ is the standard deviation.

The SNR was calculated by:

$$SNR = J_s/J_n$$

where J_s is the net X-ray generated current density and J_n is the standard deviation of the photocurrent density under X-ray exposure.

The sensitivity of our device with different applied voltages can be calculated by the equation:

$$R_s = \frac{I_p - I_d}{D \times A}$$

where R_s is the sensitivity, I_p and I_d are the photocurrent and dark current, respectively, and D and A represent the irradiation dose rate and effective area of the X-ray detector, respectively

The mobility-lifetime ($\mu\tau$) product was obtained by fitting the curve of photocurrent versus bias voltage dependence using the modified Hecht equation:

$$I = \frac{I_0 \mu \tau V}{L^2} \frac{1 - exp\left(-\frac{L^2}{\mu \tau V}\right)}{1 + \frac{Ls}{V\mu}}$$

where I_0 is the saturated photocurrent, L is the distance between the electrodes, V is the applied bias, μ is the carrier mobility, τ is the lifetime, and s is the surface recombination rate.

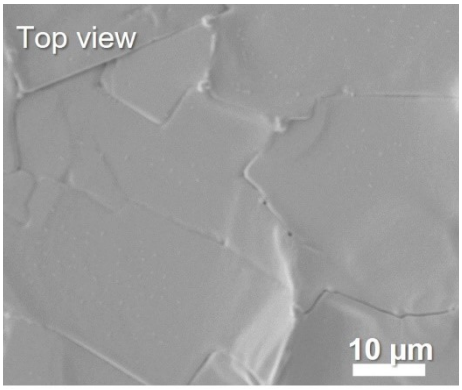

Figure S1. SEM image of the $CsPbBr_3/Cs_4PbBr_6$ film from top view.

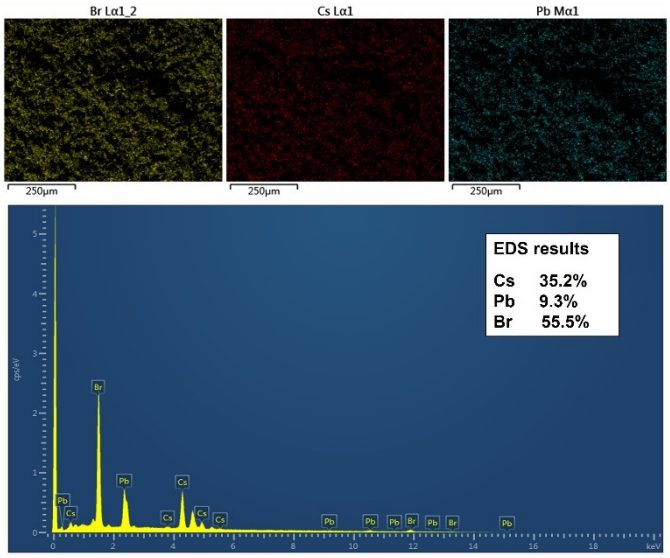

Figure S2. EDS mapping results of the composition Cs_4PbBr_6.

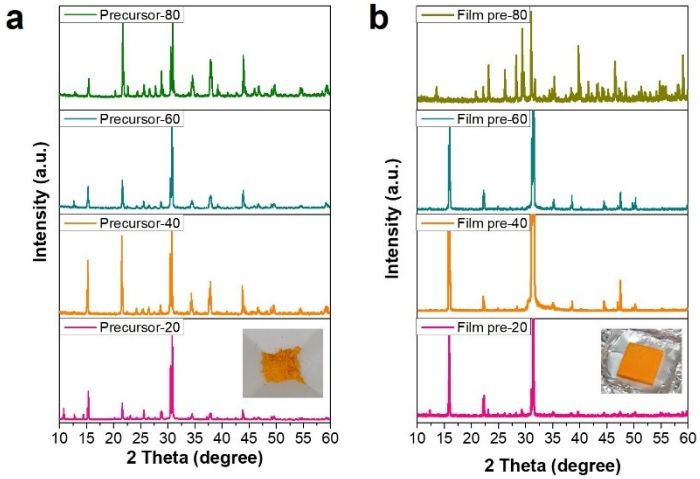

Figure S3. XRD patterns of the (a) precursor powders synthesized by different temperature 20/40/60/80 °C and (b) perovskite film after hot-pressing

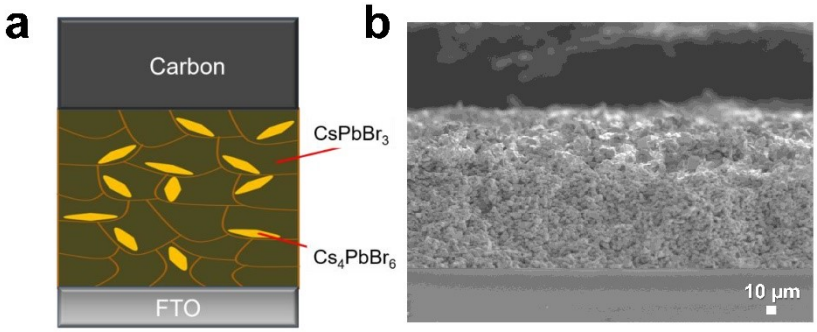

Figure S4. (a) Schematic device structure and (b) SEM images of $CsPbBr_3/Cs_4PbBr_6$ composites film rather than the layer heterojunction from cross-section view.

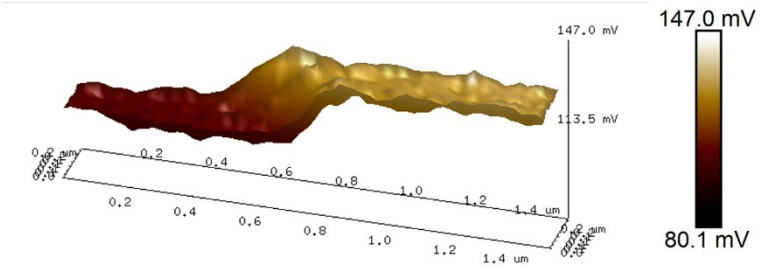

Figure S5. KPFM 3D maps of the heterojunction film at the interface.

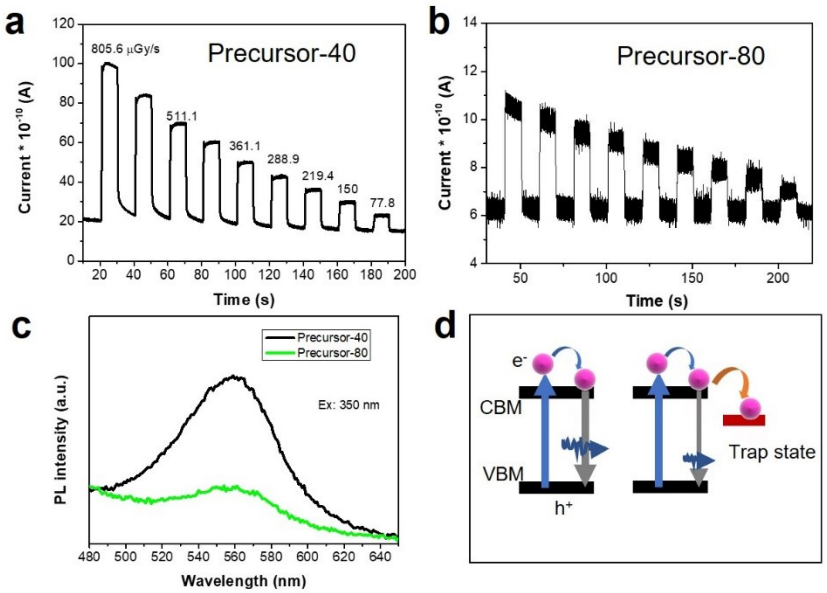

Figure S6. (a, b) X-ray i-t curves of the devices produced by different precursor powders. (c) PL results of the different precursors. (d) Schematic of the carriers recombination.

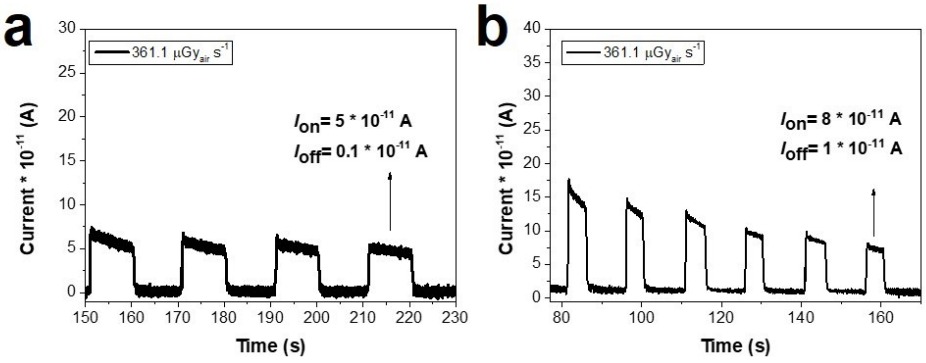

Figure S7. X-ray i-t curves of the $CsPbBr_3/Cs_4PbBr_6$ devices reach to (a) 50 and (b) 8 I_{on}/I_{off} ratio with electric field (a) 0.5V/mm and (b) 1 V/mm, respectively.

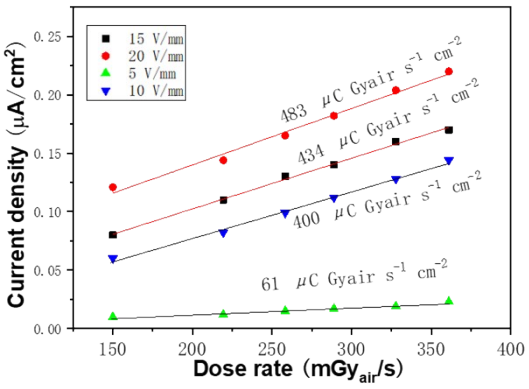

Figure S8. A linear dependence for the sensitivity is consistently observed in low-field/low-dose.

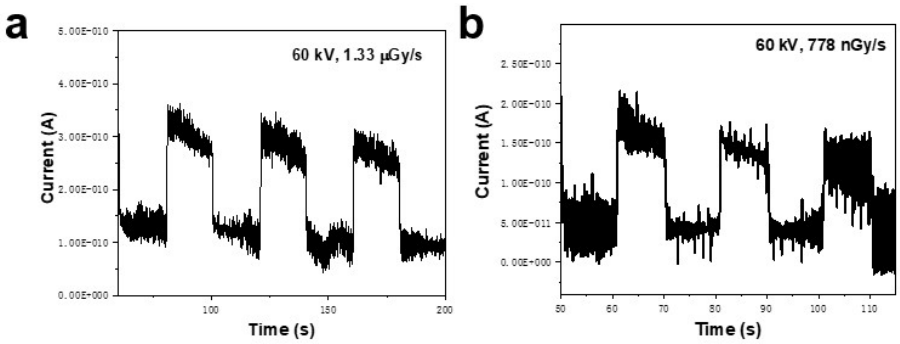

Figure S9. X-ray response current of the $CsPbBr_3/Cs_4PbBr_6$ X-ray detector under low-dose X-ray irradiation.

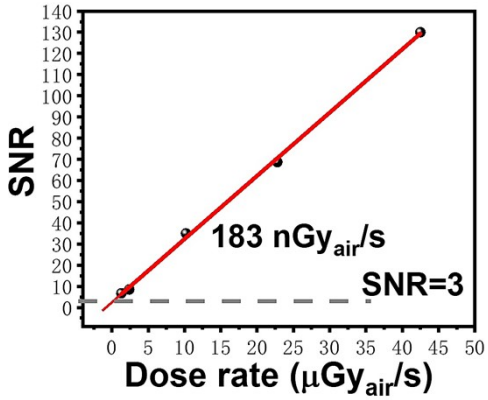

Figure S10. SNR of the $CsPbBr_3/Cs_4PbBr_6$ perovskite X-ray detector as a function of X-ray dose rate

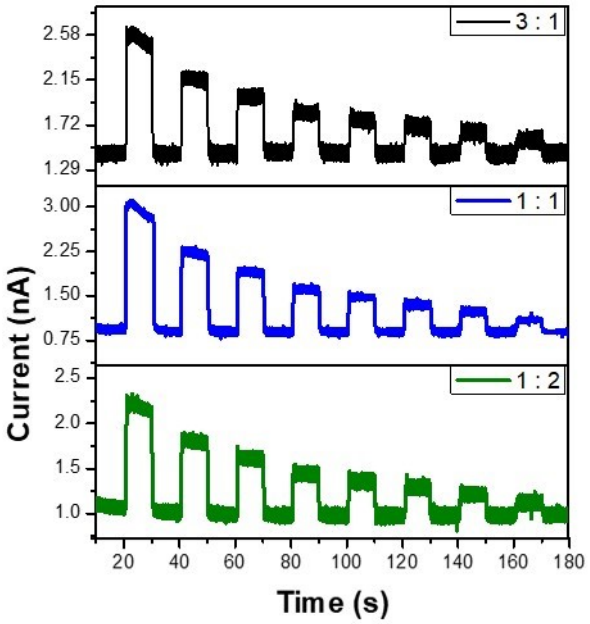

Figure S11. X-ray i-t curves of the different devices with heterojunction ratio 1:2, 1:1 and 3:1, respectively. The electric field is 2 V mm^{-1}

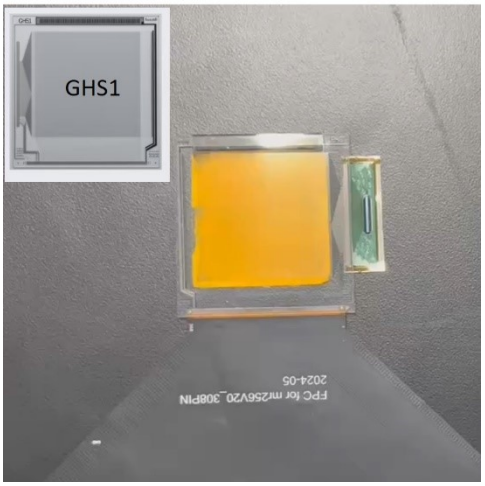

Figure S12. Digital photo of integrated $CsPbBr_3/Cs_4PbBr_6$ FPD after blading the carbon electrode and bonding with a flexible printed circuit (FPC). The orange film is $CsPbBr_3/Cs_4PbBr_6$ heterojunction (The black carbon electrode is on the backside of the perovskite thick film and is not visible from above figure. The specific device structure can be referred to Figure 3c in the main text). The inset picture is the TFT based backplane (Model: GHS1).

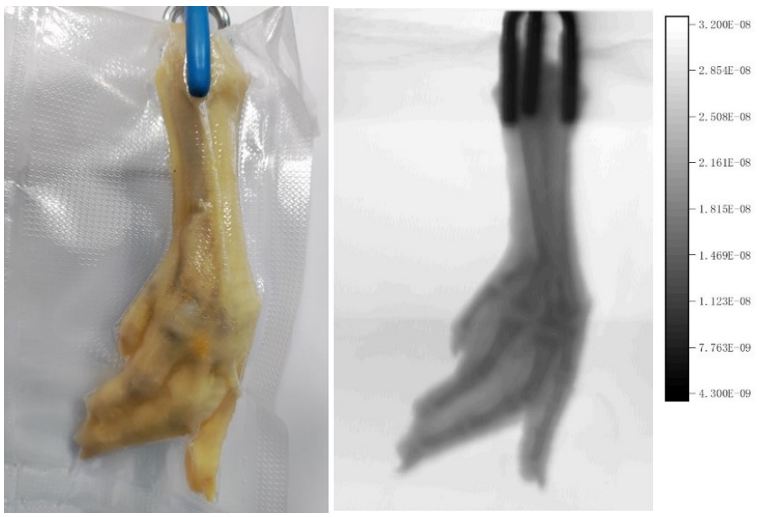

Figure S13. The X-ray images obtained with a single-pixel detector (1 × 2 mm^2) by scanning the X and Y directions at the dose rates 185.2 $\mu Gy_{air}\ s^{-1}$ (total dose: 1667 mGy_{air}, exposure time: 9000 s)

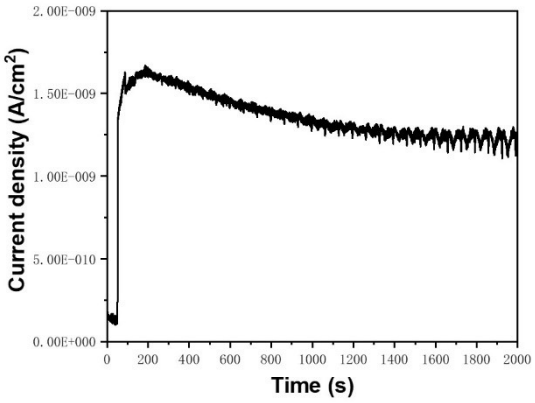

Figure 14. Stability of the annealed $CsPbBr_3/Cs_4PbBr_6$ X-ray detector under continuous X-ray radiation measured at room temperature (28 °C) and 50% relative humidity.

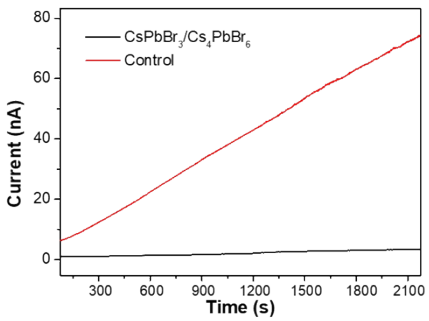

Figure S15. The temporal baseline tracking of the perovskite heterojunction and control sample devices at 100 V/mm.

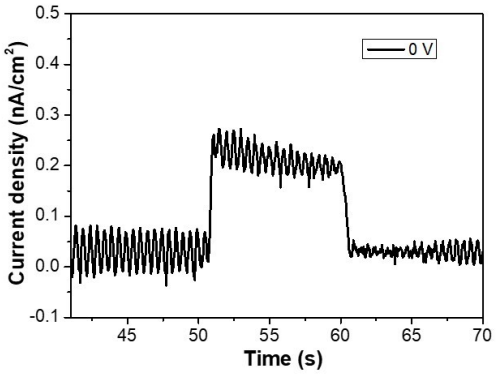

Figure S16. X-ray i-t curves (under 0 V/mm electric field) of the devices.

Table S1. The effect of precursor control details on film morphology. The reaction temperature refers to the temperature at which the precursor is synthesized in the first step. The impurity content refers to other components in the $CsPbBr_3$ precursor powder, such as Cs_4PbBr_6 hetero-phase. The approximate content was estimated by rietveld analysis of XRD diffraction peaks.

Samples	**Pre-20**	**Pre-40**	**Pre-60**	**Pre-80**
Reaction Temperature	20 °C	40 °C	60 °C	80 °C
Impurity Amount	10%	4%	30%	80%
Film Morphology	Heterojunction	Heterojunction	Heterojunction	Compounds

Table S2. Comparation of the device parameters.

Parameter	**α-Se**	**HgI_2**	**CdTe**	**$MAPbI_3$**	**This work**
Sensitivity ($\mu C\ Gy^{-1}_{air}\ cm^{-2}$)	20 [1]	1600	318	9300 [3]	12910
$\mu\tau$ ($cm^{-2}\ V^{-1}$)	10^{-7} [2]	10^{-4}	10^{-2}	2×10^{-4} [3]	10^{-7}

Table S3. Performance comparison of similar X-ray detectors reported.

	I_{on}/I_{off} ratio	Dark	Sensitivity (μC	$\mu\tau$	nt (cm^{-}	LoD	Refe

		Current	Gy_{air}^{-1} cm^{-2})	product (cm^2 /V)	^{3})	(nGy_{air} s^{-1})	renc e
Au/$CsPbBr_3$/FTO	3 (N/A)	2.0 * 10^{-7} A/cm^2	55684 (5 V/ mm)	5.1 * 10^{-3}	1.5 * 10^{10}	215	12
C/$CsPbBr_3$/SnO_2/FTO	6 (80 V/ mm, 686 μGy_{air} s^{-1})	5.0 * 10^{-6} A/cm^2	15891 (80 V/ mm);	5.2 * 10^{-4}	8.4 * 10^{10}	321	13
Au/CPB3/CP2B5/Au	4 (1 V, 204 μGy_{air} s^{-1})	1.0 * 10^{-8} A/ cm^2	258000 (25 V/ mm); 3075 (2 V/ mm)	3.4 * 10^{-3}	7.7 * 10^{9}	128	14
Au/Al/BCP/C60/$CsPbBr_3$/Au	4 (40V, 1.86 μGy_{air} s^{-1})	1.5 * 10^{-9} A/ cm^2	73000 (100 V/ mm)	2.3 * 10^{-3}	N/A	15	15
C/$CsPbBr_3$/FTO	25 (1.6V/ mm, 361 μGy_{air} s^{-1})	2.8 * 10^{-9} A/cm^2	42000 (40 V/ mm); 153 (1.6 V/ mm)	3.0 * 10^{-5}	1.5 * 10^{13}	136	16
C/$CsPbBr_3$/Cs_4PbBr_6/FTO	50 (0.5 V/ mm, 361 μGy_{air} s^{-1}), 8 (1V/ mm)	1 * 10^{-11} A/cm^2	12910 (80 V/ mm); 400 (10 V/ mm)	6.7 * 10^{-7}	3.1 * 10^{11}	183	This wor k

Table S4. The X-ray detector parameters for heterojunction devices with different ratio.

Heterojunction ratio	Dark Current (nA/cm^2)	Sensitivity (μC $Gyair^{-1}$ cm^{-2})	$I_{On/Off}$ ratio
3:1	1.5	6.7	1.5
1:1	0.9	12.4	2.4
1:2	1.0	7.8	1.8

References:

1. Jinsong Huang, *Sci. Adv.* 2021. **7**, eabg6716.
2. Jinsong Huang, *Nat. Commun.* 2019, ***10***, 1066.
3. Sarah Deumel, *Nat. Electron.*, 2011, **4**, 681–688.
4. Jin Jang, *Nanoscale*, 2018,**10**, 8591-8599.
5. Caofeng Pan, *Adv. Optical Mater.* 2023, **11**, 2202428.

6. Lena Yadgarov, *Adv. Energy Sustainability Res.*, **5**: 2300193.
7. Angshuman Nag, *ACS Energy Lett*. 2016, **1**, 4, 665–671.
8. Bo Zou, *Nat. Commun.* 2018, **9**, 4506.
9. Jongnam Park*, Adv. Sci*. 2022, **9**, 2104660.
10. Koushik Biswas, *J. Phys. Chem. Lett.* 2018, **9**, 4, 830–836.
11. Xuhui Sun, *Adv. Funct. Mater.* 2021, **31**, 2105051.
12. J. Tang, *Adv. Mater.* 2019, **31**, 1904405.
13. Y. Ge, *Nat. Comm.,* 2024, **15**:1588.
14. J. Ye, *Adv. Funct. Mater.* 2024, **34**, 2401220.
15. S. Yang, *ACS Appl. Mater. Interfaces* 2023, **15**, 44, 51370–51379.
16. Jian Wang, *Adv. Sci.* 2024, **11**, 2407314.